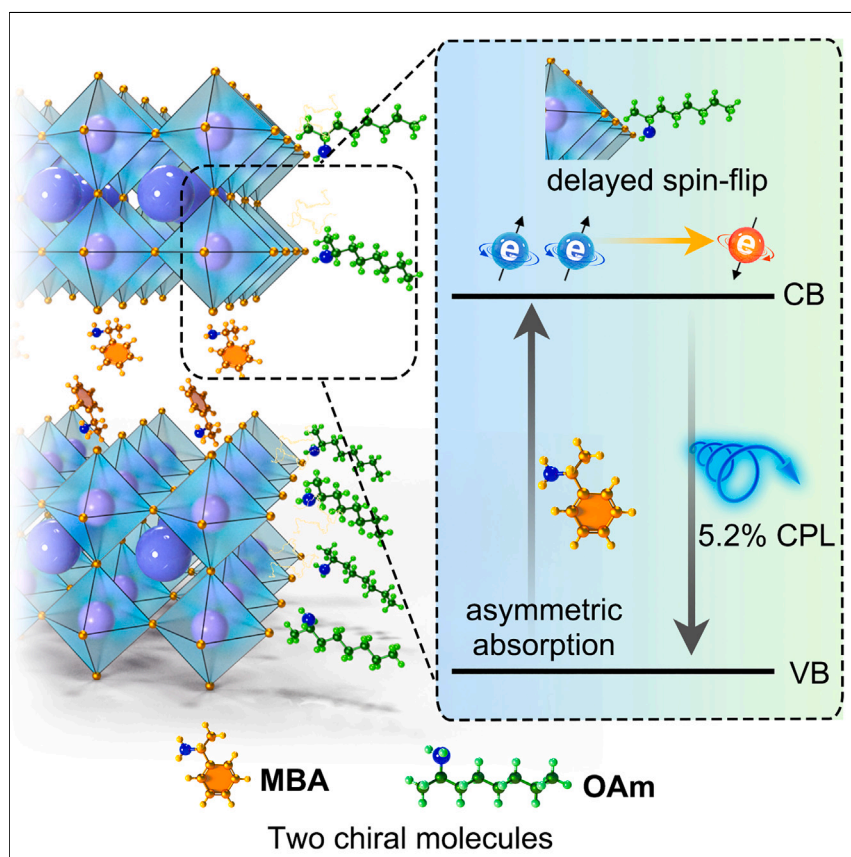


Article

Room temperature circularly polarized emission in perovskite nanocrystals through bichiral-molecule-induced lattice reconstruction



By employing a chiral spacer in the crystal lattice and another chiral ligand on the surface of perovskite nanocrystals, we enhance asymmetric light absorption and delay the spin flip of photogenerated charge carriers. The coexistence of two types of chiral molecules in low-dimensional perovskite nanocrystals leads to a CPL signal at room temperature. We also demonstrate the use of these bichiral perovskite nanoscintillators to improve the reactivity and enantioselectivity of asymmetric photopolymerization under X-ray irradiation.

Chenlu He, Jian Qiu, Zhen Mu, ..., Xian Qin, Guichuan Xing, Xiaogang Liu

gcxing@um.edu.mo (G.X.)
chmlx@nus.edu.sg (X.L.)

Highlights

Bichiral molecules collaborate to boost perovskite-based CPL

Degree of polarization up to 5.2% at room temperature with high thermal stability

Ultrafast spectroscopy reveals time-resolved spintronics

Bichiral perovskite nanoscintillators initiate asymmetric photopolymerization

**Discovery**

A new material or phenomena

He et al., Matter 7, 1–10
February 7, 2024 © 2023 Elsevier Inc.
<https://doi.org/10.1016/j.matt.2023.12.007>

Article

Room temperature circularly polarized emission in perovskite nanocrystals through bichiral-molecule-induced lattice reconstruction

Chenlu He,^{1,6} Jian Qiu,^{1,2,6} Zhen Mu,^{1,6} Jiaye Chen,¹ Yiming Wu,³ Zhengzhi Jiang,¹ Pinzheng Zhang,¹ Xian Qin,⁴ Guichuan Xing,^{5,*} and Xiaogang Liu^{1,2,3,7,*}

SUMMARY

Circularly polarized luminescence in halide organic-inorganic perovskite nanocrystals is attainable using chiral organic components. However, this phenomenon is typically restricted to cryogenic conditions due to exciton spin-flip processes. Here, we present a chiral-molecule-mediated lattice reconstruction method to induce circularly polarized luminescence in hybrid perovskite nanocrystals at room temperature. By employing a chiral spacer in the crystal lattice and another chiral ligand on the crystal surface, we enhance asymmetric light absorption and delay the spin flip of photogenerated charge carriers, as confirmed by circularly polarized pump-probe transient absorption spectroscopy. This cooperative interaction among chiral molecules results in circularly polarized emission with a polarization degree of 5.2% in mixed-phase perovskite nanocrystals. We demonstrate the application of chiral perovskites as nanoscintillators, where X-ray-induced asymmetric photopolymerization is achieved at room temperature through emitted circularly polarized radioluminescence. This property facilitates controlled *in situ* asymmetric photochemical reactions, fostering advancements in materials, drug delivery, and bioengineering applications.

INTRODUCTION

Halide organic-inorganic perovskites are promising alternatives to conventional semiconductors for a variety of applications, such as solar cells, lasers, light-emitting diodes, and photodetectors^{1–4}. These materials offer several advantages, including high defect tolerance, solution processability, and ease of optoelectronic modulation.^{5–10} Due to their predominantly ionic lattice and relatively soft crystal structure, halide perovskites can accommodate various dopants and organic molecules.¹¹ In particular, the generation of chiral perovskites by incorporating chiral organic molecules into the host scaffold has attracted considerable research interest, as the resulting chiral structures could serve as a source of circularly polarized luminescence (CPL) that facilitates the development of smart optoelectronics and spintronics.^{12,13}

Chiral spacers, such as R/S-methylbenzylamine (R/S-MBA), are frequently employed to synthesize chiral perovskite films with intrinsic circular dichroism (CD). These spacers can impose symmetry constraints on the atomic geometry, resulting in chiral perovskite structures that exhibit unique CPL properties under cryogenic conditions.^{14,15} To date, two-dimensional chiral perovskites have exhibited the highest degree of polarization ($P = 17.6\%$) at 77 K.¹⁶ In another study, a polarization of approximately 11% was observed for chiral perovskite films with low geometric

PROGRESS AND POTENTIAL

Chiral perovskite nanocrystals are promising for optoelectronics and spintronics due to their circularly polarized luminescence (CPL). However, these materials often lose their CPL properties at room temperature. This work reports a simple method to create bichiral perovskite nanocrystals that maintain their CPL at room temperature. By combining chiral interior spacers and surface ligands, these nanocrystals develop a chiral structure that significantly enhances light absorption asymmetry. Moreover, the surface ligands can suppress the spin flip of the photogenerated charge carriers. The coexistence of large asymmetric light absorption (circular dichroism) and the inhibition of spin-flip of carriers contributes to a CPL signal with 5.2% circular polarization. These nanocrystals have the potential to enhance the enantioselectivity of asymmetric photopolymerization under X-ray irradiation.

dimensionality and a mixed-phase structure at 2 K in a 7 T magnetic field.¹⁷ Despite the success, the CPL signal decreases significantly with increasing temperature, resulting in unpolarized emission at room temperature. This phenomenon is mainly attributed to the thermally activated spin flip of excitons, which occurs independently of the structural chirality of the perovskite lattice.¹⁸ In this regard, it is vital to develop a simple and effective approach to suppress exciton spin flipping in chiral perovskites at room temperature.

CPL signals are usually obtained by introducing chiral ligands to nanocrystal surfaces.^{19,20} This induces chirality transfer by coupling the static dipole of chiral ligands with the transition dipole moment of the nanocrystals.²¹ Although the atomic structure of the core remains achiral, the chiral-ligand-induced electrical field on the surface regulates the electronic distribution and generates CPL.²² For example, using chiral ligands, perovskite nanocrystals can achieve a room temperature circular polarization of 3.4%, attributable to the chiral-induced spin selectivity (CISS).²³ The temperature-stable CISS effect demonstrates the strong coupling between molecular chirality and electron spin, providing a promising technique to achieve CPL in achiral nanomaterials at room temperature.²⁴ Nevertheless, the intrinsic CD signal of perovskite nanocrystals is extremely weak, which makes it difficult to distinguish and utilize left- and right-handed photons.^{25,26}

In this work, we demonstrate a facile and cost-effective synthesis of chiral perovskite nanocrystals of formamidinium lead bromide (FAPbBr₃) with room temperature CPL through the cooperation between chiral interior spacers and chiral surface ligands. The introduction of R/S-MBA spacers into nanocrystals creates chiral crystal lattices, resulting in greater asymmetric light absorption. Moreover, chiral R/S-2-octylamines (R/S-OAms) are employed as surface ligands to hinder the spin flip of excitons (Figure 1). The coexistence of large asymmetric absorption and suppressed spin flip leads to a CPL signal with 5.2% circular polarization, the highest ever observed in perovskite nanocrystals at room temperature.^{27–30} We also demonstrate the use of these chiral perovskite nanoscintillators to improve the reactivity and enantioselectivity of asymmetric photopolymerization at room temperature under X-ray irradiation.

RESULTS AND DISCUSSION

Structural features of low-dimensional perovskite nanocrystals

In a typical experiment, we prepared low-dimensional FAPbBr₃ nanocrystals by intercalating molecular spacers (MBA⁺ cations) between the planes of [PbBr₆]^{4–} octahedra. The presence of MBA⁺ within FAPbBr₃ nanocrystals was confirmed by solid-state ¹H nuclear magnetic resonance (NMR) spectroscopy, as evidenced by the NMR signals at about 5.3 ppm, while undoped FAPbBr₃ showed signals above 6.0 ppm (Figures 2A and 2B).³¹ It is noteworthy that protons on the chiral carbon of MBA⁺ are responsible for the NMR signals of ~5.3 ppm in the MBA-doped sample. This MBA intercalation was further characterized by two-dimensional (2D) solid-state NMR spectroscopy (Figures 2C and S1). Moreover, the use of MBA resulted in the formation of large, low-dimensional mixed-phase nanocrystals, while undoped controls produced 3D monodisperse nanocubes of approximately 15 nm.^{32,33} In addition, high-resolution transmission electron microscopy (HRTEM) was used to confirm the incorporation of MBA⁺ into the perovskite lattice. In the case of the conventional 3D FAPbBr₃, the HRTEM image of a single particle showed a lattice spacing of 3.0 Å, which could be assigned to the (200) plane of cubic nanocrystals. In contrast, the MBA-doped low-dimensional nanocrystals exhibited an increased interplanar spacing of about 5.2 Å, which could be assigned to the n = 3 (200) plane.³⁴

¹Department of Chemistry, National University of Singapore, Singapore 117549, Singapore

²Joint School of National University of Singapore and Tianjin University, International Campus of Tianjin University, Binhai New City, Fuzhou 350207, China

³Institute of Materials Research and Engineering, Agency for Science, Technology and Research (A*STAR), Singapore 138634, Singapore

⁴Strait Institute of Flexible Electronics (SIFE Future Technologies), Fujian Normal University, Fuzhou 350117, China

⁵Joint Key Laboratory of the Ministry of Education, Institute of Applied Physics and Materials Engineering, University of Macau, Avenida da Universidade, Taipa, Macau 999078, China

⁶These authors contributed equally

⁷Lead contact

*Correspondence: gcxing@um.edu.mo (G.X.), chmlx@nus.edu.sg (X.L.)

<https://doi.org/10.1016/j.matt.2023.12.007>

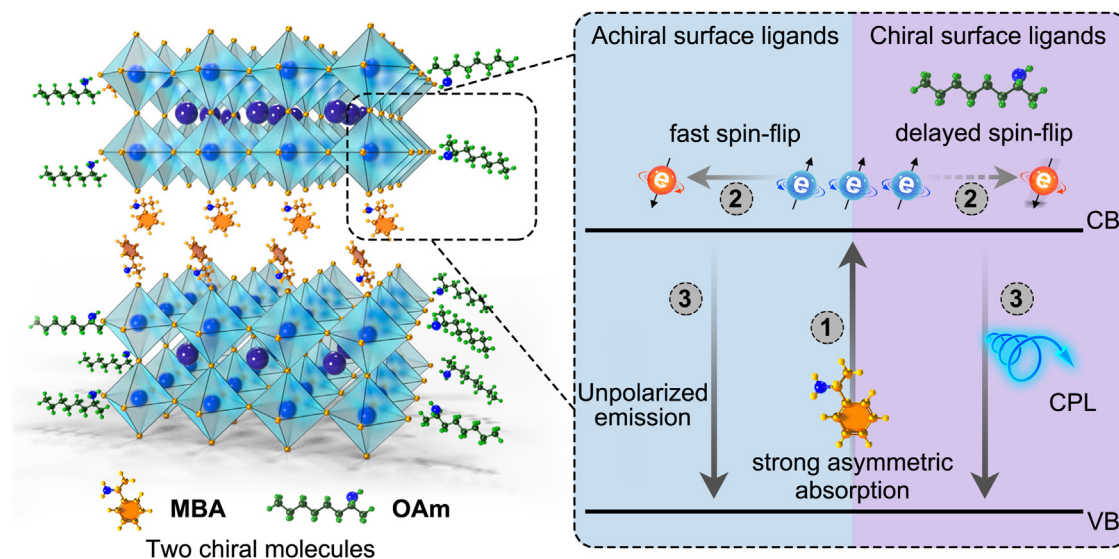


Figure 1. Design of bichiral perovskite nanocrystals for room temperature CPL

In our design, two types of chiral molecules are used to grow chiral perovskite nanocrystals: methylbenzylamine (MBA; in orange) spacers are inserted into nanocrystal lattices, while 2-octylamines (OAm; in green) molecules modify nanocrystal surfaces. Because of the cooperation between the two, asymmetric light absorption increases and exciton spin flipping is suppressed, contributing to enhanced room temperature CPL. CB, conduction band; VB, valence band.

X-ray diffraction (XRD) investigations of 3D FAPbBr₃ nanocrystals displayed characteristic diffraction peaks at 2θ of approximately 15° and 30°, corresponding to the (001) and (002) planes, respectively, of typical cubic nanocrystals (Figure 2E). However, MBA-doped nanocrystals exhibited diffraction peaks below 15°, which was consistent with layered crystal structures.³⁵ Furthermore, we constructed an MBA-intercalated FAPbBr₃ atomic supercell in which a bilayer MBA was inserted into the (001) planes of [PbBr₆]⁴⁻ octahedra, followed by structural optimization by first-principles calculations based on density functional theory (DFT). The intercalation of MBA increased the vertical distance between the [PbBr₆]⁴⁻ inorganic layers by ~87% (Figures 2D and S2; Table S1), which was close to the increase in the lattice spacing evidenced by XRD. The interaction between MBA and the inorganic frameworks was dominated by H–Br hydrogen bonding.³⁶ Moreover, the MBA intercalation induced a strong rotation of neighboring FA⁺ molecules. These distinct differences in crystal structure and morphology confirmed the successful formation of low-dimensional nanocrystals using the MBA spacer.^{37–39} The low-dimensional MBA-FAPbBr₃ displays enhanced quantum confinement, which effectively mitigates ion migration and the self-doping effect, consequently leading to improved intrinsic stability (Figures S3 and S4).

Optical properties of bichiral perovskite nanocrystals

These MBA-doped low-dimensional nanocrystals showed a large band gap and multiple quantum well structures, similar to low-dimensional polycrystalline perovskite films (Figures 3A–3C).^{40–42} The high miscibility of chiral MBA and OAm molecules allowed for the fabrication of four types of chiral nanocrystals with unique chiroptical signatures in CD spectroscopy: SS, SR, RS, and RR, where the first letter denotes the chiral configuration of the spacer MBA and the latter denotes the chiral configuration of the surface ligand OAm. Compared to the CD signals of MBA or OAm in the UV region, we observed characteristic bisignate CD signals of SS and RR nanocrystals at the corresponding absorption band in the UV-visible (UV-vis) region (Figures 3D and S5). The

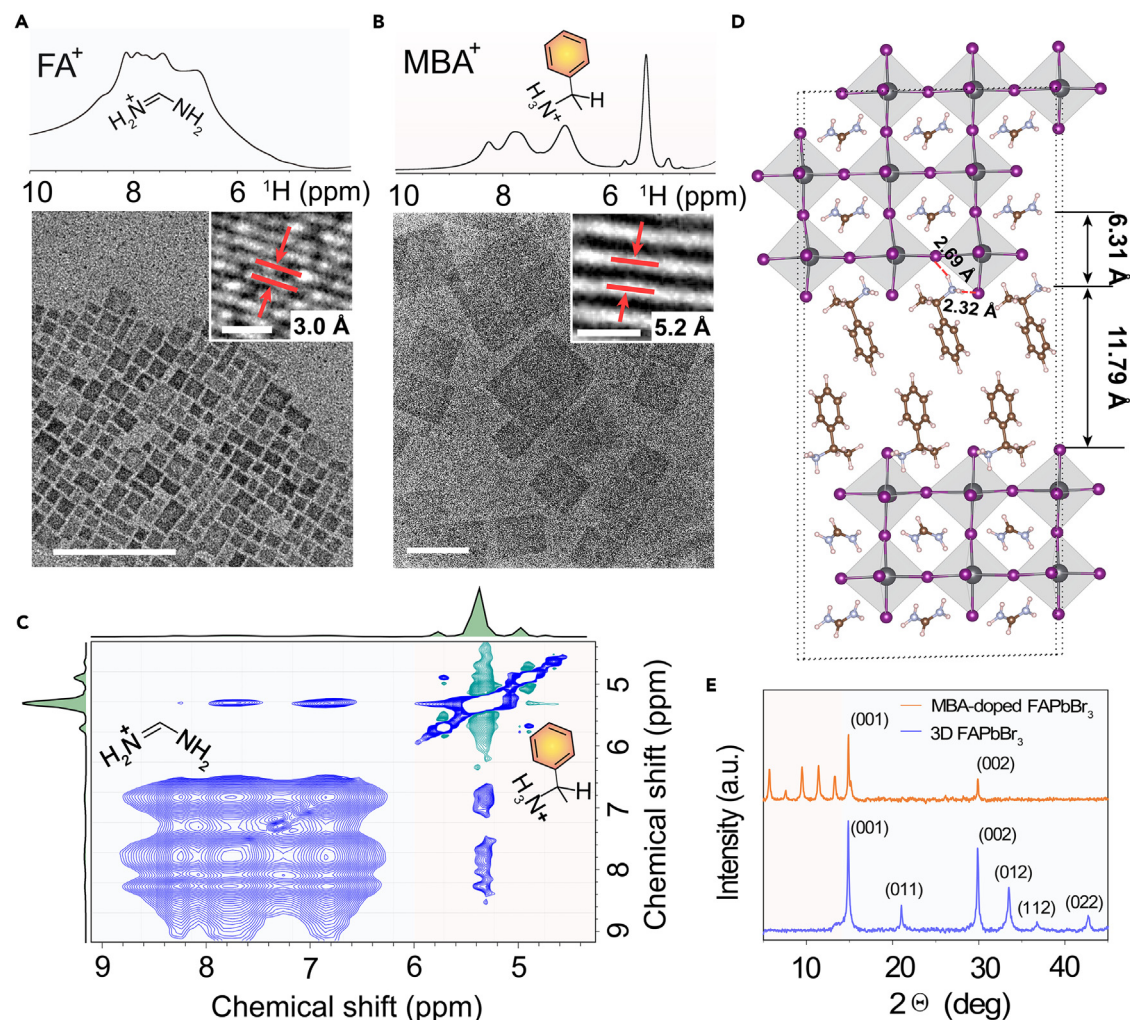


Figure 2. Structural characterization of perovskite nanocrystals

(A and B) ^1H NMR spectra and TEM images of FAPbBr₃ and MBA-doped FAPbBr₃ nanocrystals, respectively. Scale bar: 100 nm. Insets are the corresponding HRTEM images. Scale bar: 1 nm.

(C) 2D solid-state NMR spectra of MBA-doped FAPbBr₃ nanocrystals. The MBA⁺/FA⁺ value is approximately 11% through analyzing the integrated area of the NMR peaks.

(D) Optimized atomic structure of MBA-doped FAPbBr₃. Purple, silver, brown, gray, and white balls denote bromide, lead, carbon, nitrogen, and hydrogen atoms, respectively.

(E) XRD patterns of MBA-doped and undoped FAPbBr₃ nanocrystals.

optical activity was likely induced by the chirality transfer from organic molecules to inorganic scaffolds. Specifically, the SS nanocrystals showed a positive Cotton effect with a maximum signal at ~ 465 nm and a crossover at ~ 354 nm. When RR nanocrystals were tested, the corresponding CD spectrum reversed signs due to the mirror symmetry of these two samples. In addition, the optical activity could be influenced by the cooperative interactions between the chiral MBA and OAm molecules, which can be quantified by the anisotropy factor g_{abs} .⁴³ SS or RR nanocrystals exhibited a high level of asymmetry, with a maximum $|g_{\text{abs}}|$ of about 2.0×10^{-3} , whereas the SR or RS nanocrystals displayed a weaker Cotton effect with a maximum $|g_{\text{abs}}|$ of about 0.5×10^{-3} . This observation suggests that the coexistence of two types of chiral organic molecules with identical chiral configurations enhances the nanocrystal's intrinsic chirality, essential for achieving a high degree of polarization in CPL.

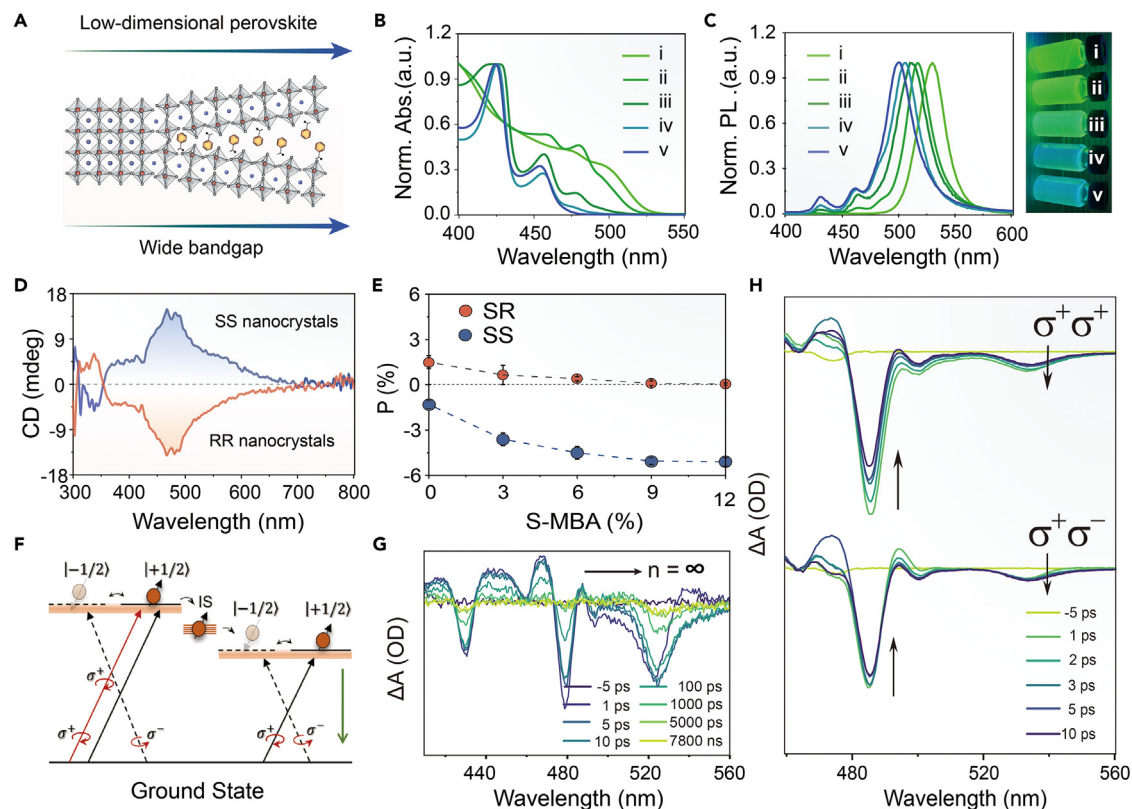


Figure 3. Optical characterizations of bichiral perovskite nanocrystals

(A) Schematic showing a dimensional reduction from 3D to low dimensions through MBA doping.

(B and C) Photoluminescence ($\lambda_{\text{ex}} = 365 \text{ nm}$) and UV-vis spectra of nanocrystals with MBA at various concentrations: (i–v) 0%, 3%, 6%, 9%, and 12%, respectively. Right: corresponding photograph of nanocrystals under 365 nm excitation.

(D) CD spectra of SS and RR nanocrystals.

(E) Degrees of polarization of SR and SS nanocrystals with various S-MBA doping contents. Error bars are defined as standard deviations of $n = 3$ independent measurements.

(F) Illustration of spin transfer in MBA-doped perovskite nanocrystals. IS, intermediate state.

(G) Transient absorption spectra of MBA-doped mixed-phase perovskite nanocrystals (pumped at 400 nm).

(H) Circularly polarized pump-probe transient absorption spectra of RR perovskite nanocrystals (pumped at 475 nm).

We next investigated the characteristics of CPL in SS and SR nanocrystals at room temperature. Using a linearly polarized 405 nm laser, we recorded polarization-resolved photoluminescence spectra of nanocrystals with different proportions of S-MBA molecules (Figures S6–S8).¹⁶ We found that 3D nanocrystals modified only with R-OAm or S-OAm molecules generated left-handed or right-handed CPL with an averaged $|P|$ value of $\sim 1\%$ at room temperature. Notably, the addition of S-MBA resulted in a contrasting maximum $|P|$ value of 5.2% for SS nanocrystals, while their SR counterparts showed a $|P|$ value of 0 (Figure 3E). These results suggest that the enhanced asymmetric light absorption and the suppressed exciton spin flipping contribute to CPL.

The dynamics of photogenerated charge carriers in the MBA-doped nanocrystals was investigated by transient absorption (TA) spectroscopy at room temperature, revealing a distinct energy transfer process from the low-dimensional to the high-dimensional phase (Figure 3G).⁴⁴ The RR perovskite nanocrystals exhibited two bleaching peaks at 485 (PB1) and 530 nm (PB2), corresponding to the low-dimensional phase ($n = 3$) and the 3D phase ($n = \infty$), respectively.⁴⁵ We further examined

spin transfer using circularly polarized pump-probe TA (CP-TA) spectroscopy (Figures 3F and 3H).^{46–48} The upper curve was recorded under a right-handed circularly polarized pump with a right-handed circularly polarized probe ($\sigma^+\sigma^+$), while the lower curve was obtained using a right-handed circularly polarized pump with a left-handed circularly polarized probe ($\sigma^+\sigma^-$). In the case of $\sigma^+\sigma^+$, the bleaching peaks at 485 nm exhibited a rapid rise within 5 ps, which can be attributed to the selective excitation of spin-up electrons by the pump σ^+ . This resulted in a non-equilibrium population of spin-up and spin-down electrons in the excited state. The excess spin-up electrons subsequently underwent spin relaxation by which the spin direction of the electrons flipped downward and an equilibrium spin population was reached. In contrast, the lower curve recorded under the $\sigma^+\sigma^-$ conditions characterized the inverse process, where rapid state filling occurred, as evidenced by a negative upward signal within the initial 5 ps. This ultrafast spin relaxation characteristic was observed in both RR and RS perovskite nanocrystals at PB1 and PB2 bleaching peaks (Figure S9). Lifetime fitting revealed that the spin relaxation occurred on a longer timescale (~ 3.0 ps) than energy transfer (~ 0.3 ps) from low- to high-dimensional phases, supporting the possibility of simultaneous spin transfer and energy transfer during rapid charge carrier formation in mixed-phase perovskite nanocrystals (Figure S10).

Next, we investigated the spin coherence of charge carriers in chiral OAm-modified perovskite nanocrystals at room temperature. By applying polarized pumping with polarized probes ($\sigma^+\sigma^+$ and $\sigma^+\sigma^-$), the OAm-modified nanocrystals showed distinct carrier dynamics near the exciton bleaching peak, indicating ligand-modulated spin relaxation of charge carriers (Figure 4A). Moreover, power-dependent experiments indicate that nanocrystals modified with chiral OAm have a longer spin relaxation time than those modified with achiral OAm (Figures 4B and S11). The spin lifetime of nanocrystals modified with achiral OAm decreased gradually from ~ 2 to ~ 0.8 ps with increasing carrier density, which is consistent with previous reports.²⁴ In contrast, the spin lifetime of nanocrystals modified with chiral OAm also decreased with carrier density but remained longer (~ 3 – 1.6 ps) than that of their counterparts modified with achiral OAm, suggesting that the suppressed spin flip was attributed to surface chiral ligands through CISS.

Asymmetric photopolymerization triggered by bichiral perovskite nanoscintillators

The CPL of bichiral perovskite nanocrystals has the potential to induce asymmetric photopolymerization of achiral diacetylene monomers under X-ray irradiation at room temperature. The diacetylene monomer in the solid state showed an intense absorption below 200 nm (Figure S12), indicating that photopolymerization could be initiated by X-rays to generate conjugated polydiacetylene. However, X-rays alone cannot induce CPL-responsive asymmetric photopolymerization, as this requires specific waveplates that can convert X-rays into circularly polarized light, which presents a significant manufacturing challenge. To overcome this issue, bichiral perovskite nanocrystals synthesized with two types of chiral molecules can be used as chiral scintillators to emit circularly polarized radioluminescence upon X-ray irradiation.

The photopolymerization was carried out by exposing a hybrid film of diacetylene monomers with bichiral perovskite nanoscintillators (yellow film in Figure 4C) over an X-ray source. This film turned blue with intense absorption maximums at about 650 nm, thus confirming the formation of polydiacetylene.⁴³ With the use of chiral SS scintillators as the structural symmetry breaker, the resulting hybrid

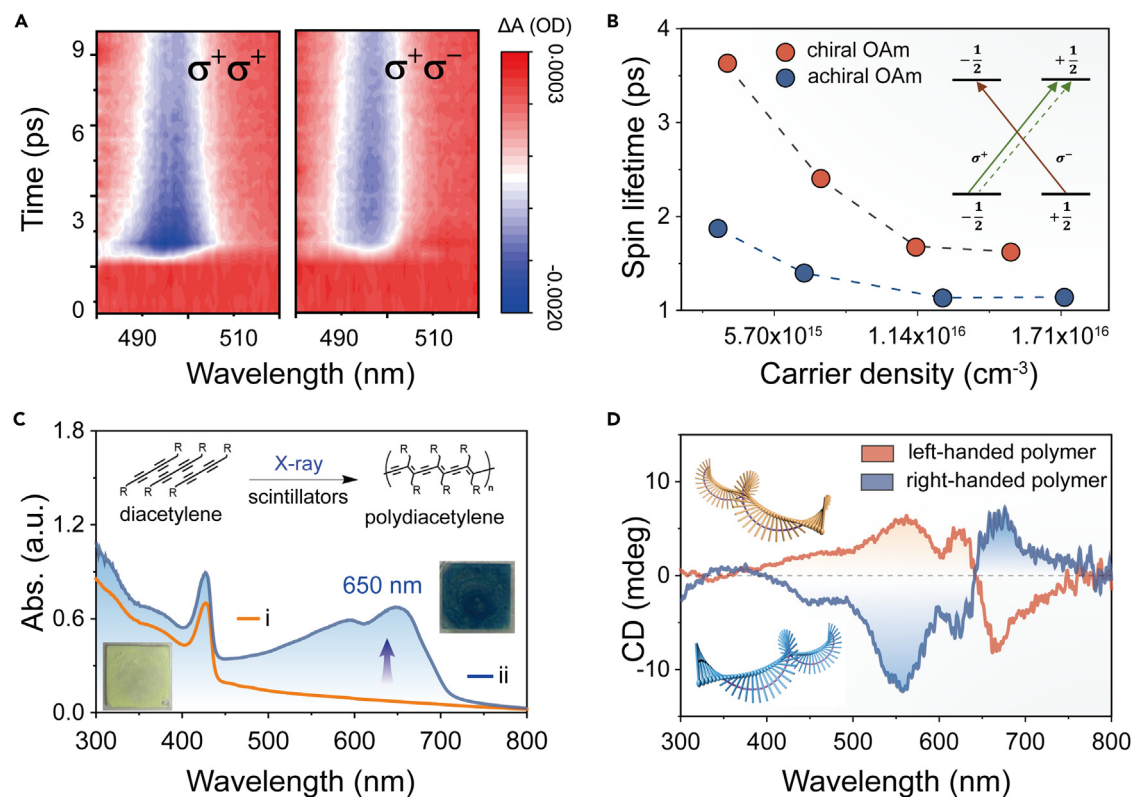


Figure 4. Spin dynamics and asymmetric photopolymerization of perovskite nanocrystals

(A) Spin dynamics of charge carriers in nanocrystals modified with chiral OAm ligands under σ^+ pump and σ^+ probe and under σ^+ pump and σ^- probe. (B) Power-dependent spin-coherence lifetime of nanocrystals modified with chiral OAm or achiral OAm ligands. Inset is the mechanistic illustration of spin-coherence lifetime measurement. The probe σ^+ selectively detects the change in spin polarization. The flip of a spin would simultaneously lead to a decay of the σ^+ bleach and a formation of the σ^- bleach. (C) UV-vis spectra and illustration of solid-state photopolymerization of diacetylene monomer under X-ray irradiation assisted with bichiral perovskite nanoscintillators. The insets show the hybrid film (i) before and (ii) after photopolymerization. (D) CD spectra and illustration of left- and right-handed polydiacetylenes induced by chiral RR and SS perovskite nanoscintillators. The insets depict left- and right-handed polydiacetylene chains.

polydiacetylene films showed a right-handed polymer configuration and exhibited optical activity, as proven by the positive Cotton effect (Figure 4D). If chiral RR scintillators were used instead, the corresponding CD spectrum of resulting polydiacetylene flipped signs, indicating a predominantly left-handed polymer configuration. These results demonstrated that bichiral nanoscintillators can induce asymmetric photopolymerization under X-ray initiation, where the helical behavior of polydiacetylene chains was regulated by the CPL feature of chiral nanoscintillators. To further support this conclusion, two control experiments were performed. Firstly, polydiacetylene induced by RS and SR nanocrystals showed no chiral preference. Secondly, chiral organic molecules (MBA and OAm) were unable to generate chiral polydiacetylene under X-ray irradiation (Figure S13). Therefore, the successful break of structure symmetry in this photopolymerization can be attributed to the highly circular polarized emission from chiral nanoscintillators, which could improve the reactivity and enantioselectivity of photopolymerization (Figure S14). Moreover, by taking advantage of the very deep penetration of X-rays, asymmetric photopolymerization was achieved through materials that are challenging to penetrate with conventional UV or visible light, such as wood, polypropylene, and pig skin tissue. The resulting polymer exhibited similar CD signals with various intensities, indicating the

successful formation of chiral polydiacetylene (Figure S15). These results reveal the potential of chiral perovskite nanoscintillators to assist in X-ray-initiated asymmetric photopolymerization under challenging conditions.

Conclusions

We outlined a feasible and economical protocol to produce chiral perovskite nanocrystals with high circularly polarized emission ($P = 5.2\%$) at room temperature. The synergistic effect resulting from chiral OAm and MBA molecules functionalized in the nanocrystals leads to enhanced asymmetric light absorption and suppressed spin flip. Additionally, these bichiral perovskite scintillators were deployed as tools to induce asymmetric photopolymerization under X-ray. These findings open up new avenues for applications, in particular *in situ* asymmetric photochemical reactions within internal conditions or biological systems.

EXPERIMENTAL PROCEDURES

Resource availability

Lead contact

Further information and requests for resources should be directed to and will be fulfilled by the lead contact, Professor Xiaogang Liu (chmlx@nus.edu.sg).

Materials availability

Formamidinium acetate (FA-acetate; 99%), oleic acid (technical grade 90%), oleylamine (technical grade 70%), 1-octadecene (technical grade 90%), hexane (reagent grade $\geq 95\%$), R-MBA (98% purity), S-MBA (98% purity), and acetic acid (99% purity) were purchased from Sigma-Aldrich. Compound 10,12-pentacosadiynoic acid was purchased from Sigma-Aldrich and purified by being dissolved in hexane, followed by filtration to remove the polymer before use. R-OAm (98% purity) and (S)-2-octylamine (S-OAm; 98% purity) were purchased from Alfa Aesar.

Data and code availability

All relevant data that support the findings of this work are available from the corresponding author upon reasonable request.

CHARACTERIZATIONS

All UV-vis spectra were recorded using an Agilent Cary 3500 spectrophotometer. Photoluminescence was recorded using a fluorescence spectrometer (FLSP920; Edinburgh Instruments, Livingston, UK) equipped with an Xe lamp. Powder XRD patterns were tested using a Bruker D8 Advance diffractometer with graphite-monochromatized $\text{CuK}\alpha$ radiation ($\lambda = 0.15406$ nm). TEM images were acquired using a JEOL JEM-3011 transmission electron microscope operated at 300 kV. HRTEM images were filtered using the ABSF Filter (average background subtracted filter) implemented by Digital Micrograph. CD spectra were measured using a JASCO CD J-815 spectrometer.

SUPPLEMENTAL INFORMATION

Supplemental information can be found online at <https://doi.org/10.1016/j.matt.2023.12.007>.

ACKNOWLEDGMENTS

This research was primarily funded through the National Research Foundation, the Prime Minister's Office of Singapore under its Competitive Research Program (CRP award no. NRF-CRP23-2019-0002), the NRF Investigatorship Programme

(award no.NRF-NRFI05-2019-0003), the Science and Technology Development Fund, Macao SAR (file nos.0082/2021/A2 and 006/2022/ALC), UM's research fund (file nos. MYRG2022-00241-IAPME and MYRG-CRG2022-00009-FHS), and the Natural Science Foundation of China (61935017 and 62175268).

AUTHOR CONTRIBUTIONS

C.H. and J.Q. prepared the samples. Z.M. and Z.J. performed optical measurements. X.Q. performed DFT calculations. J.C. and P.Z. were responsible for TEM characterizations. X.L. and G.X. conceived the experiment and managed the research. X.Q., Y.W., G.X., and X.L. analyzed and discussed the results and wrote the manuscript.

DECLARATION OF INTERESTS

The authors declare no competing interests.

Received: September 16, 2023

Revised: November 16, 2023

Accepted: December 6, 2023

Published: January 11, 2024

REFERENCES

- Xiang, W., and Tress, W. (2019). Review on recent progress of all-inorganic metal halide perovskites and solar cells. *Adv. Mater.* *31*, 1902851.
- Qin, C., Sandanayaka, A.S.D., Zhao, C., Matsushima, T., Zhang, D., Fujihara, T., and Adachi, C. (2020). Stable room-temperature continuous-wave lasing in quasi-2D perovskite films. *Nature* *585*, 53–57.
- Han, D., Imran, M., Zhang, M., Chang, S., Wu, X.G., Zhang, X., Tang, J., Wang, M., Ali, S., Li, X., et al. (2018). Efficient light-emitting diodes based on in situ fabricated FAPbBr₃ nanocrystals: the enhancing role of the ligand-assisted reprecipitation process. *ACS Nano* *12*, 8808–8816.
- Dong, Y., Zhang, Y., Li, X., Feng, Y., Zhang, H., and Xu, J. (2019). Chiral perovskites: promising materials toward next-generation optoelectronics. *Small* *15*, 1902237.
- Akkerman, Q.A., Rainò, G., Kovalenko, M.V., and Manna, L. (2018). Genesis, challenges and opportunities for colloidal lead halide perovskite nanocrystals. *Nat. Mater.* *17*, 394–405.
- Shamsi, J., Urban, A.S., Imran, M., De Trizio, L., and Manna, L. (2019). Metal halide perovskite nanocrystals: synthesis, post-synthesis modifications, and their optical properties. *Chem. Rev.* *119*, 3296–3348.
- Almeida, G., Goldoni, L., Akkerman, Q., Dang, Z., Khan, A.H., Marras, S., Moreels, I., and Manna, L. (2018). Role of acid–base equilibria in the size, shape, and phase control of cesium lead bromide nanocrystals. *ACS Nano* *12*, 1704–1711.
- Wang, H., Ye, F., Sun, J., Wang, Z., Zhang, C., Qian, J., Zhang, X., Choy, W.C.H., Sun, X.W., Wang, K., and Zhao, W. (2022). Efficient CsPbBr₃ nanoplatelet-based blue light-emitting diodes enabled by engineered surface ligands. *ACS Energy Lett.* *7*, 1137–1145.
- Dong, Y., Qiao, T., Kim, D., Parobek, D., Rossi, D., and Son, D.H. (2018). Precise control of quantum confinement in cesium lead halide perovskite quantum dots via thermodynamic equilibrium. *Nano Lett.* *18*, 3716–3722.
- Bohn, B.J., Tong, Y., Gramlich, M., Lai, M.L., Döbbling, M., Wang, K., Hoye, R.L.Z., Müller-Buschbaum, P., Stranks, S.D., Urban, A.S., et al. (2018). Boosting tunable blue luminescence of halide perovskite nanoplatelets through postsynthetic surface trap repair. *Nano Lett.* *18*, 5231–5238.
- Long, G., Sabatini, R., Saidaminov, M.I., Lakhwani, G., Rasmita, A., Liu, X., Sargent, E.H., and Gao, W. (2020). Chiral-perovskite optoelectronics. *Nat. Rev. Mater.* *5*, 423–439.
- Wei, Q., and Ning, Z. (2021). Chiral perovskite spin-optoelectronics and spintronics: toward judicious design and application. *ACS Mater. Lett.* *3*, 1266–1275.
- Ma, S., Ahn, J., and Moon, J. (2021). Chiral perovskites for next-generation photonics: from chirality transfer to chiroptical activity. *Adv. Mater.* *33*, 2005760.
- Ahn, J., Lee, E., Tan, J., Yang, W., Kim, B., and Moon, J. (2017). A new class of chiral semiconductors: chiral-organic-molecule-incorporating organic-inorganic hybrid perovskites. *Mater. Horiz.* *4*, 851–856.
- Lu, H., Xiao, C., Song, R., Li, T., Maughan, A.E., Levin, A., Brunecky, R., Berry, J.J., Mitzi, D.B., Blum, V., and Beard, M.C. (2020). Highly distorted chiral two-dimensional tin iodide perovskites for spin polarized charge transport. *J. Am. Chem. Soc.* *142*, 13030–13040.
- Ma, J., Fang, C., Chen, C., Jin, L., Wang, J., Wang, S., Tang, J., and Li, D. (2019). Chiral 2D perovskites with a high degree of circularly polarized photoluminescence. *ACS Nano* *13*, 3659–3665.
- Long, G., Jiang, C., Sabatini, R., Yang, Z., Wei, M., Quan, L.N., Liang, Q., Rasmita, A., Askerka, M., Walters, G., et al. (2018). Spin control in reduced-dimensional chiral perovskites. *Nat. Photonics* *12*, 528–533.
- Chen, Y., Ma, J., Liu, Z., Li, J., Duan, X., and Li, D. (2020). Manipulation of valley pseudospin by selective spin injection in chiral two-dimensional perovskite/monolayer transition metal dichalcogenide heterostructures. *ACS Nano* *14*, 15154–15160.
- Xu, L., Wang, X., Wang, W., Sun, M., Choi, W.J., Kim, J.Y., Hao, C., Li, S., Qu, A., Lu, M., et al. (2022). Enantiomer-dependent immunological response to chiral nanoparticles. *Nature* *601*, 366–373.
- Sujith, M., Vishnu, E.K., Sappati, S., Oliyantakath Hassan, M.S., Vijayan, V., and Thomas, K.G. (2022). Ligand-induced ground- and excited-state chirality in silicon nanoparticles: surface interactions matter. *J. Am. Chem. Soc.* *144*, 5074–5086.
- Forde, A., Ghosh, D., Kilin, D., Evans, A.C., Tretiak, S., and Neukirch, A.J. (2022). Induced chirality in halide perovskite clusters through surface chemistry. *J. Phys. Chem. Lett.* *13*, 686–693.
- Ma, W., Xu, L., de Moura, A.F., Wu, X., Kuang, H., Xu, C., and Kotov, N.A. (2017). Chiral inorganic nanostructures. *Chem. Rev.* *117*, 8041–8093.
- Kim, Y.-H., Zhai, Y., Gaubing, E.A., Habisreutinger, S.N., Moot, T., Rosales, B.A., Lu, H., Hazarika, A., Brunecky, R., Wheeler, L.M., et al. (2020). Strategies to achieve high circularly polarized luminescence from colloidal organic-inorganic hybrid perovskite nanocrystals. *ACS Nano* *14*, 8816–8825.

24. Kim, Y.-H., Zhai, Y., Lu, H., Pan, X., Xiao, C., Gaulding, E.A., Harvey, S.P., Berry, J.J., Vardeny, Z.V., Luther, J.M., and Beard, M.C. (2021). Chiral-induced spin selectivity enables a room-temperature spin light-emitting diode. *Science* **371**, 1129–1133.
25. Crassous, J., Fuchter, M.J., Freedman, D.E., Kotov, N.A., Moon, J., Beard, M.C., and Feldmann, S. (2023). Materials for chiral light control. *Nat. Rev. Mater.* **8**, 365–371.
26. Naaman, R., Paltiel, Y., and Waldeck, D.H. (2019). Chiral molecules and the electron spin. *Nat. Rev. Chem.* **3**, 250–260.
27. Gao, J.X., Zhang, W.Y., Wu, Z.G., Zheng, Y.X., and Fu, D.W. (2020). Enantiomorphic perovskite ferroelectrics with circularly polarized luminescence. *J. Am. Chem. Soc.* **142**, 4756–4761.
28. Liu, Y., Luo, Z., Wei, Y., C, Li, C, Li, Y, Chen, X, He, X, Chang, and Z, Quan (2023). Integrating achiral and chiral organic ligands in zero-dimensional hybrid metal halides to boost circularly polarized luminescence. *Angew. Chem. Int. Ed.* **135**, e202306821.
29. Jin, K.H., Zhang, Y., Li, K.J., Sun, M.E., Dong, X.Y., Wang, Q.L., and Zang, S.Q. (2022). Enantiomorphic single crystals of linear lead (II) bromide perovskitoids with white circularly polarized emission. *Angew. Chem. Int. Ed.* **61**, e202205317.
30. Liu, D.Y., Li, H.Y., Han, R.P., Liu, H.L., and Zang, S.Q. (2023). Multiple stimuli-responsive luminescent chiral hybrid antimony chlorides for anti-counterfeiting and encryption applications. *Angew. Chem. Int. Ed.* **62**, e202307875.
31. Lu, H., Liu, Y., Ahlawat, P., Mishra, A., Tress, W.R., Eickemeyer, F.T., Yang, Y., Fu, F., Wang, Z., Avalos, C.E., et al. (2020). Vapor-assisted deposition of highly efficient, stable black-phase FAPbI₃ perovskite solar cells. *Science* **370**, eabb8985.
32. Wang, H., Xu, W., Wei, Q., Peng, S., Shang, Y., Jiang, X., Yu, D., Wang, K., Pu, R., Zhao, C., et al. (2023). In-situ growth of low-dimensional perovskite-based insular nanocrystals for highly efficient light emitting diodes. *Light Sci. Appl.* **12**, 62.
33. Xu, W., Ji, R., Liu, P., Cheng, L., Zhu, L., Zhang, J., Chen, H., Tong, Y., Zhang, C., Kuang, Z., et al. (2020). In situ-fabricated perovskite nanocrystals for deep-blue light-emitting diodes. *J. Phys. Chem. Lett.* **11**, 10348–10353.
34. Xu, Z., Lu, D., Liu, F., Lai, H., Wan, X., Zhang, X., Liu, Y., and Chen, Y. (2020). Phase distribution and carrier dynamics in multiple-ring aromatic spacer-based two-dimensional Ruddlesden–Popper perovskite solar cells. *ACS Nano* **14**, 4871–4881.
35. Liang, C., Gu, H., Xia, Y., Wang, Z., Liu, X., Xia, J., Zuo, S., Hu, Y., Gao, X., Hui, W., et al. (2020). Two-dimensional Ruddlesden–Popper layered perovskite solar cells based on phase-pure thin films. *Nat. Energy* **6**, 38–45.
36. Ma, S., Jung, Y.K., Ahn, J., Kyhm, J., Tan, J., Lee, H., Jang, G., Lee, C.U., Walsh, A., and Moon, J. (2022). Elucidating the origin of chiroptical activity in chiral 2D perovskites through nano-confined growth. *Nat. Commun.* **13**, 3259.
37. Cao, D.H., Stoumpos, C.C., Yokoyama, T., Logsdon, J.L., Song, T.B., Farha, O.K., Wasielewski, M.R., Hupp, J.T., and Kanatzidis, M.G. (2017). Thin films and solar cells based on semiconducting two-dimensional ruddlesden–popper (CH₃(CH₂)₂NH₃)₂(CH₃NH₃)_{n-1}Sn_nI_{3n+1} perovskites. *ACS Energy Lett.* **2**, 982–990.
38. Yu, Y., Zhang, D., and Yang, P. (2017). Ruddlesden–Popper phase in two-dimensional inorganic halide perovskites: a plausible model and the supporting observations. *Nano Lett.* **17**, 5489–5494.
39. Deng, W., Jin, X., Lv, Y., Zhang, X., Zhang, X., and Jie, J. (2019). 2D Ruddlesden–Popper perovskite nanoplate based deep-blue light-emitting diodes for light communication. *Adv. Funct. Mater.* **29**, 1903861.
40. Liao, Y., Liu, H., Zhou, W., Yang, D., Shang, Y., Shi, Z., Li, B., Jiang, X., Zhang, L., Quan, L.N., et al. (2017). Highly oriented low-dimensional tin halide perovskites with enhanced stability and photovoltaic performance. *J. Am. Chem. Soc.* **139**, 6693–6699.
41. Liu, J., Leng, J., Wu, K., Zhang, J., and Jin, S. (2017). Observation of internal photoinduced electron and hole separation in hybrid two-dimensional perovskite films. *J. Am. Chem. Soc.* **139**, 1432–1435.
42. Zhou, N., Shen, Y., Li, L., Tan, S., Liu, N., Zheng, G., Chen, Q., and Zhou, H. (2018). Exploration of crystallization kinetics in quasi two-dimensional perovskite and high performance solar cells. *J. Am. Chem. Soc.* **140**, 459–465.
43. He, C., Feng, Z., Shan, S., Wang, M., Chen, X., and Zou, G. (2020). Highly enantioselective photo-polymerization enhanced by chiral nanoparticles and in situ photopatterning of chirality. *Nat. Commun.* **11**, 1188.
44. Chen, X., Lu, H., Wang, K., Zhai, Y., Lunin, V., Sercel, P.C., and Beard, M.C. (2021). Tuning spin-polarized lifetime in two-dimensional metal-halide perovskite through exciton binding energy. *J. Am. Chem. Soc.* **143**, 19438–19445.
45. Giovanni, D., Lim, J.W.M., Yuan, Z., Lim, S.S., Righetto, M., Qing, J., Zhang, Q., Dewi, H.A., Gao, F., Mhaisalkar, S.G., et al. (2019). Ultrafast long-range spin-funneling in solution-processed Ruddlesden–Popper halide perovskites. *Nat. Commun.* **10**, 3456.
46. Giovanni, D., Ma, H., Chua, J., Grätzel, M., Ramesh, R., Mhaisalkar, S., Mathews, N., and Sum, T.C. (2015). Highly spin-polarized carrier dynamics and ultralarge photoinduced magnetization in CH₃NH₃PbI₃ perovskite thin films. *Nano Lett.* **15**, 1553–1558.
47. Lin, X., Han, Y., Zhu, J., and Wu, K. (2023). Room-temperature coherent optical manipulation of hole spins in solution-grown perovskite quantum dots. *Nat. Nanotechnol.* **18**, 124–130.
48. Liu, S., Kepenekian, M., Bodnar, S., Feldmann, S., Heindl, M.W., Fehn, N., Zerhoch, J., Shcherbakov, A., Pöthig, A., Li, Y., et al. (2023). Bright circularly polarized photoluminescence in chiral layered hybrid lead-halide perovskites. *Sci. Adv.* **9**, eadh5083.